


Strain-aided room-temperature second-order ferroelectric phase transition in monolayer PbTe: Deep potential molecular dynamics simulations

Zhanpeng Gong,¹ Jefferson Zhe Liu²,[✉] Xiangdong Ding,¹ Jun Sun,¹ and Junkai Deng^{1,*}

¹State Key Laboratory for Mechanical Behavior of Materials, Xi'an Jiaotong University, Xi'an 710049, China

²Department of Mechanical Engineering, The University of Melbourne, Parkville, Victoria 3010, Australia

 (Received 20 July 2023; revised 26 September 2023; accepted 3 October 2023; published 20 October 2023)

The discovery of room-temperature monolayer ferroelectrics (FEs) holds significant promise for advancing the development of nanoscale functional devices. Although the *ab initio* calculations have demonstrated the strain-induced ferroelectricity of two-dimensional (2D) PbTe, the structural and thermodynamic characteristics of this ferroelectric phase transition at larger temporal and spatial scales remain unexplored. Molecular dynamics (MD) is an effective tool to use to address this question. However, the lack of an appropriate force field has hindered progress. Here, we have developed an interatomic potential for 2D PbTe based on the deep potential framework, enabling MD simulations with *ab initio*-level accuracy to investigate the FE phase transition. Our MD results demonstrate robust ferroelectricity at room temperature in adequately strained 2D PbTe, which remains paraelectric at lower temperatures. Structural analyses indicate that the FE transitions are displacive, highlighting the strong coupling between the strain condition and the polarization state. Furthermore, we established a phase diagram of 2D PbTe in the temperature-strain space, guiding the tunable phase transition temperature with the aid of prestrains. Finally, the second-order transition nature of FE transition in 2D PbTe is observed, suggesting the potential utilization of a new room-temperature, nonhysteresis 2D ferroelectric material.

DOI: [10.1103/PhysRevB.108.134112](https://doi.org/10.1103/PhysRevB.108.134112)

I. INTRODUCTION

The developments of low dimensional ferroelectrics (FEs) are of great importance for meeting the demands on advanced nanoscale devices, such as FE field-effect transistors with low-power dissipation [1], high-density nonvolatile memory [2], miniaturized sensors [3,4], and microactuators [4,5]. As promising functional materials, the rise of two-dimensional (2D) materials has opened a new avenue for the discovery of 2D FEs with atomic thickness [6]. From theoretical calculations, several 2D FE materials with phosphorene-like atomic structures, including compounds [7,8] and elemental materials [9,10], have recently been proposed. Especially in group-IV chalcogenide 2D materials, the structure and the ferroelectricity [11,12] of the two-atomic layer-thick SnTe are indisputably revealed, which subsequently stimulated research on the ferroelectricity of other 2D SnTe analogs, MXs ($M = \text{Ge}, \text{Sn}; X = \text{S}, \text{Se}, \text{Te}$) [13–16]. However, the lead chalcogenide PbX ($X = \text{S}, \text{Se}, \text{and Te}$) atomic layers are intrinsically non-FE materials [11,12], although their corresponding bulk materials share the same space group ($Fm\bar{3}m$) as bulk SnTe at room temperature.

It is well established that strain engineering plays a dominant role in the control and modulation of the structural phase and related ferroelectricity for FE thin films [17]. In particular, the elastic strain has been proven to be a viable approach to induce ferroelectricity for intrinsic paraelectric (PE) SrTiO₃ thin film [18], and modulates the FE-to-PE transition temperature

in group-IV monochalcogenide monolayers [19]. This inspires us to explore the possible FE phase transition of 2D PbX via strain engineering. Recently, we discovered a strain-aided FE phase transition for monolayer PbX by using density functional theory (DFT)-based first-principles calculations [20], retaining excellent agreement with reported results [21]. It suggests a prospective means of achieving 2D FE materials in otherwise non-FE 2D PbX and designing nanoscale functional devices, taking advantage of the high strain tolerance of the 2D materials [22] and developments of the sophisticated PbX-based lateral heterostructures [23]. However, it is still highly desirable to determine the Curie temperature (T_C) of the strain-aided FE phase transition and stability of the room-temperature ferroelectricity under a specific external strain for real applications of 2D Pb chalcogenide materials.

In terms of investigating the temperature effect of the FE phase transition, classic molecular dynamics (MD) simulations have been proven to be an effective approach [24], providing a clearer atomic picture than the analytical theory method like the effective Hamiltonian [25,26]. However, due to the lack of a reliable empirical interatomic potential for 2D PbX materials, it has limited MD simulations. Recently, machine-learning potentials have demonstrated their strength in MD simulations [27]. Compared to the classic force fields, which are typically based on analytically formulated functionals, the neural network forcefields that use symmetry-preserving descriptors exhibit a significantly higher level of accuracy [28]. Several successful packages exist, including the Gaussian approximation potentials [29], the Behler-Parrinello neural network [30], moment tensor potentials [31], SchNet [32], and so forth. Among them, the deep

*Corresponding author: junkai.deng@mail.xjtu.edu.cn

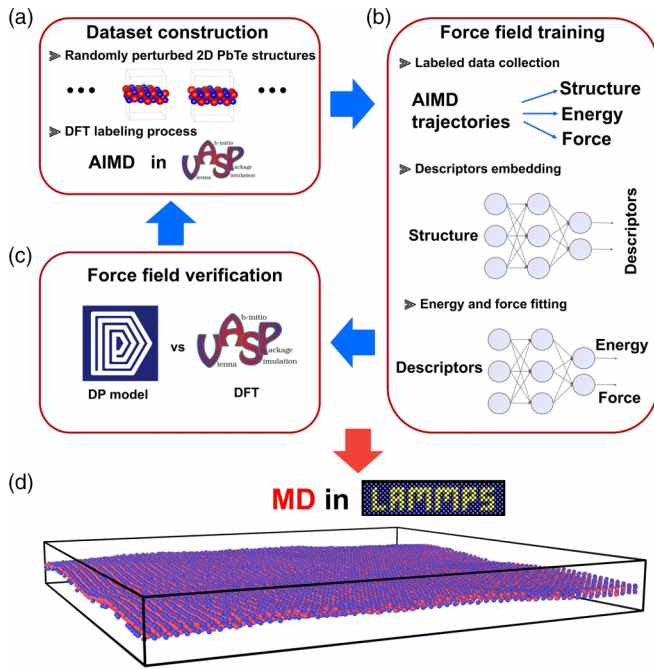


FIG. 1. Workflow of current work. (a) DFT data set based on the structures with thousands of strain conditions. Every ten steps of AIMD results, which include structures, corresponding forces, and energies, are selected as training data for the DeePMD-kit package. (b) Force field training process of DeePMD-kit package. The structures are embedded into descriptors through the embedding network, preserving the translational, rotational, and permutational symmetry of the system. The fitting network then regresses the descriptors to the corresponding energies and forces. (c) Force field verification by comparing the results between the DP model and DFT. The model will be corrected if any unreasonable results emerge. (d) Molecular dynamics simulations with the validated force field. It explores the phase transitions of 2D PbTe in the strain-temperature space.

potential (DP) model, which dynamically embeds the configurations into descriptors by neural networks [33], demonstrated the DFT-level accurate simulation results over many distinct research fields, including perovskite FEs [34–36].

In this work, we developed a DP model to investigate the strain-induced and temperature-induced ferroelectric phase transition (SIFPT and TIFPT) of 2D PbTe. The accuracy of the trained DP model was validated by successfully reproducing the DFT predictions across a larger configurational space. Employing MD simulations with the verified DP, we examined the SIFPT of 2D PbTe under varying temperatures to gain atomic-level insights into the PE-to-FE phase transition. A phase diagram was constructed in the (uniaxial tensile) strain-temperature space, revealing the tunable T_C of strain-aided 2D PbTe over a wide temperature range. Furthermore, motivated by the absence of hysteresis, we proposed that the strain-induced and temperature-induced ferroelectric phase transitions in 2D PbTe exhibit second-order phase transition characteristics.

II. COMPUTATIONAL METHODS

The workflow of this work is depicted in Fig. 1, which consists of two main components: the development of the

force field (DP model) and the MD simulations of the ferroelectric phase transition of 2D PbTe. The data set construction is the first and the most important step in this work. To explore the phase space of interest, we carefully perturbed the ground-state structures to serve as initial configurations for the *ab initio* molecular dynamics (AIMD) explorations [Fig. 1(a)]. After training the DP model [Fig. 1(b)], we tested its generalization and prediction ability over a more expansive configurational space than the training set [Fig. 1(c)]. If the performance of the DP model was inadequate, we repeated the procedure. The validated DP model was then used in the MD simulations in the LAMMPS packages (Fig. 1(d)) [37]. The simulation details are presented in the following sections. With the accurate deep-learning force field, we anticipate gaining atomic insight into the SIFPT and TIFPT of 2D PbTe.

A. The data set obtained from DFT calculations

The data set used to train the DP model was generated by employing the AIMD simulations with the Vienna *Ab initio* Simulation Package (VASP) [38,39]. The projector augmented-wave method [40,41] was used to treat core and valence electrons, and the generalized gradient approximation functional of Perdew, Burke, and Ernzerhof was applied to account for the electron exchange-correlation interaction [42]. To ensure the accuracy of the results, an energy cutoff of 500 eV, a Gaussian smearing of 0.05 eV, and a $5 \times 5 \times 1$ k -point meshing scheme were used for all the calculations. A 20-Å vacuum layer was added to the 36-atom slab to avoid the interaction of the neighboring monolayer PbTe, which represented the 2D PbTe system. The initial atomic structures contained the ground state (space group $Cmcm$) and configurations with applied specific strain perturbations of the 2D PbTe, which were fully relaxed by DFT calculations before the AIMD simulations. The phase space was then explored by running the MD simulations with NVT ensemble conditions at various temperatures ranging from 10 K to 400 K. During the ionic relaxations, the atomic positions were optimized until all atomic forces were below 10^{-2} eV Å⁻¹, and the total energy differences were less than 10^{-5} eV. These settings were verified to be suitable for studying the 2D PbTe in our previous DFT study [20] and facilitated the comparison of our results with those obtained using DFT during the validation process. The atomic configurations, the corresponding energies, and atomic forces were extracted from the AIMD trajectories every ten steps to construct the training data set. In total, about 40,000 frames of the AIMD trajectories were employed to train the DP model.

B. Training of machine-learning interatomic potential (DP model)

The DeePMD-kit package [43] is capable of constructing deep learning-based representations of potential energy surfaces to perform molecular dynamics simulations. This package has a broad range of potential applications, from finite molecules to extended systems, and from metallic systems to chemically bonded systems [44].

In the DP model, the potential energy E of an atomic configuration is represented as a sum of the atomic energy

E_i of each atom i , which is obtained from the descriptors through a fitting network. These descriptors characterize the local environment of atom i within a cutoff radius R_c of 7.5 Å. The maximum number of allowable atoms within this R_c is 95 for both lead and tellurium. To preserve the translational, rotational, and permutational symmetry of the descriptors, an embedding network is used. In addition, a smooth edition of the DP model is employed to remove the discontinuity introduced by the cutoff radius, with the inner cutoff set at 7.2 Å. The sizes of the embedding and fitting networks are (25, 50, 100) and (240, 240, 240), respectively. The loss function is defined as

$$L(p_\epsilon, p_f, p_\xi) = p_\epsilon \Delta\epsilon^2 + \frac{p_f}{3N} \sum_i |\Delta F_i|^2 + \frac{p_\xi}{9} \|\Delta\xi\|^2,$$

where $\Delta\epsilon$, ΔF_i , and $\Delta\xi$ represent the differences in energy, force, and virial tensor between the predictions of the DP model and the DFT data. The p_ϵ , p_f , and p_ξ are weight coefficients of energy, force, and virial tensor, respectively. During the training procedure, the p_ϵ increases from 0.02 to 1; meanwhile, the p_f decreases from 1000 to 1. The p_ξ is zero as the virial tensor was unused in this work. After the DP model was trained for 6 000 000 steps, various tests were performed to validate its accuracy.

C. MD simulations

Using the well-tested DP model, equilibrium MD simulations were carried out with periodic boundary conditions using LAMMPS packages [37], within the temperature range of 10 K to 400 K. Same as the DFT setting, the vacuum layer of at least 20 Å was added to the monolayer PbTe in all MD simulations. To eliminate the potential size effect, a sufficiently large supercell ($60 \times 60 \times 12$ D PbTe, 14 400 atoms) was used to obtain the converged results. The phase space trajectory was determined using the velocity Verlet algorithm with a time step of 1 fs. The temperature and pressure were controlled by the Nosé-Hoover thermostat and Parrinello-Rahman barostat, respectively [45,46]. The so-called quasistatic loading procedure was employed with a temperature and strain interval of 1 K and 0.1% (engineering strain), respectively. To get reliable information on the phase transition, at each loading, the total energies of the systems were first converged in the equilibrium run of 10 ps, and the configurations used for the analysis were subsequently sampled in the production run of 20 ps. For a better investigation of the PE-to-FE phase transition, the summation (u_i) of the offset (\vec{R}_i) of the nearest lead and tellurium atoms in each unit cell i was monitored:

$$u_i = \sum_{\text{unitcell}} \vec{R}_i.$$

The atomic velocities and positions were collected every 1ps for the calculation of the offset (\vec{R}_i). The free-energy profile of the 2D PbTe during the phase transition was accurately calculated by the well-tempered metadynamics [47,48] at 300 K, using the uniaxial strain as the collective variable.

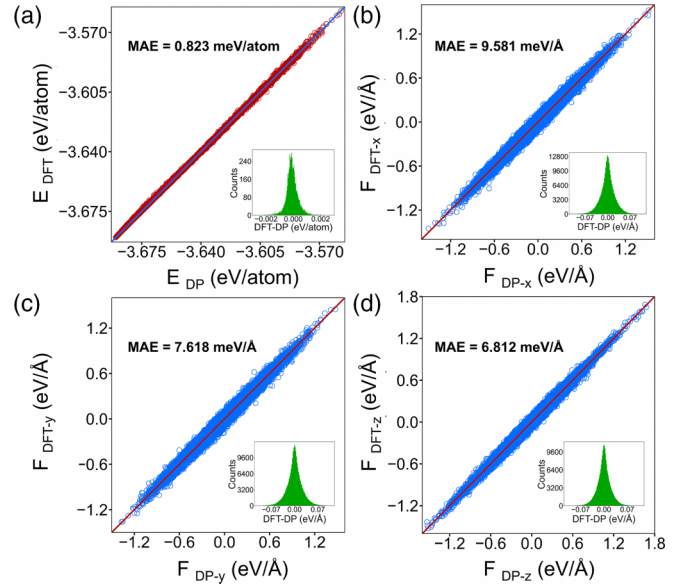


FIG. 2. Comparisons of the energies and forces between the DFT and DP model over the structures sampled from the temperature range of 10 K to 400 K. Energies per atom (a) and atomic forces [(b), (c), and (d) for the pseudo- x , $-y$, and $-z$ directions, respectively] of the structures that are not included in the training data set. The insets show the distributions of the absolute errors and the lines show the perfect correlations of the corresponding variables.

III. RESULTS AND DISCUSSION

A. Verification of the DP model

We evaluated the predictive capability of our DP model on a validation set consisting of 10 000 frames of AIMD trajectories. Figure 2 shows a comparison between the predictions of the DP model and the DFT calculations on the energies and atomic forces under different strain conditions in the temperature range of 10 K to 400 K. The insets of Fig. 2 show the corresponding absolute errors. The small mean absolute errors (MAEs) obtained on the configurations not included in the training set (0.823 meV/atom, 9.581 meV/Å, 7.618 meV/Å, and 6.812 meV/Å for the energy, force X , force Y , and force Z , respectively) demonstrate the good generalization performance of our DP model.

We then compared the predictions of our DP model for the static properties of 2D PbTe with DFT results, verifying the accuracy of our predictions for lattice constants and the critical strain of phase transition, which are 4.636 Å and 3.80%, respectively, with errors within 0.5% of DFT results (4.638 Å and 3.75%). The ability of our DP model to predict energy under the complex strain conditions was also verified and yielded accurate and concordant predictions of energies with a MAE of 1.2 meV/atom, as shown in Supplemental Material Fig. S1 [49]. Furthermore, our DP model achieved a small MAE of 1.44 meV/atom when compared to the DFT results for the strain-energy plot of the configurations with different equal biaxial strains, as provided in Supplemental Material Fig. S2 [49].

We also calculate the phonon dispersion spectrum using both our DP model and DFT calculations (density functional perturbation theory in VASP and Phonopy [50]), with

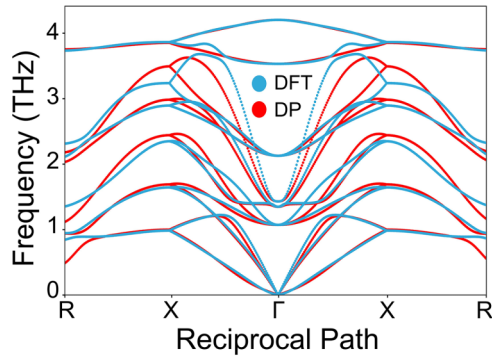


FIG. 3. The comparison of phonon dispersion spectrums of monolayer 2D PbTe calculated by DFT and the DP model, respectively.

a comparison shown in Fig. 3. Overall, the phonon dispersion relationship provided by the DP model agrees well with the DFT result, although it shows some discrepancies in the optical mode. These discrepancies may be due to the differences between the potential energy surfaces, which are amplified in the case of the phonon dispersion relationships because of their close correlations to the second-order derivatives of the potential energy surface. The DFT spectrum is calculated in the ground state at 0 K, whereas our DP model is trained on an AIMD data set with a temperature range of 10 K to 400 K. Therefore, the energy surfaces could have minor differences between our DP model and DFT calculations.

The in-plane FE polarization of 2D PbTe is characterized by the offset of lead and tellurium atoms in the ab plane. It is significant to gain insight into the energy landscape of the strained 2D PbTe concerning the offsets of atoms. In the uniaxial case, we considered only the a -strained case due to the fourfold symmetry in the ab plane of 2D PbTe, and the b -strained one can be obtained easily by symmetry manipulation. We used a prestrain of 4%, which is slightly larger than the critical strain for phase transition of 2D PbTe in the DFT results (3.75%) [20,21], for better illustration. The results of

the DFT calculations and the DP model predictions are shown in Fig. 4. The DP model [Fig. 4(b)] accurately reproduces the characteristics of the energy landscape revealed by DFT [Fig. 4(a)], including two degenerate FE states for the uniaxial case and a double well, with the MAE of 1.01 meV/atom. These results demonstrate that our DP model can capture the energy features of the FE polarization of strained 2D PbTe, which is crucial for investigating SIFPT.

B. Strain-induced ferroelectric phase transition at ambient conditions

By performing the MD simulations with the DP model, the SIFPT at a finite temperature was investigated, which yielded atomic-level insights. The soft mode theory is an effective tool for elucidating the structural changes occurring during the FE phase transition [51–53]. In our previous work utilizing DFT, we confirmed the SIFPT of 2D PbTe when subjected to uniaxial strain [20]. It is observed that the softening of an unstable zone-center polar mode is associated with the structural variation in this phase transition, and its eigenmode corresponds to the displacement of the nearest lead and tellurium atoms within the plane [20]. The displacement, denoted as offset u_i can thus be regarded as the local mode of the specific unit cell [26]. Consequently, the polarization associated with the local mode in the unit cell i is $P_i = Z^* u_i / S_{\text{cell}}$. Here, Z^* is the Born effective charge of the local mode [26]. In 2D PbTe, Z^* was determined by the DFT calculations and found to be 6.062. Furthermore, for the 2D scenario, we employed the in-plane area of the unit cell (S_{cell}) instead of volume to define the dipole density. Supplemental Material Fig. S3 [49] presents a comparison between the polarizations obtained by the local mode and Berry phase [54], demonstrating a good consistency between the two methods.

As the prospect of 2D room-temperature FE holds great appeal for developing miniature functional devices [7,12,55], we investigated the potential of the room-temperature FE in 2D PbTe under accessible strain. We performed MD simulations of 2D PbTe at 300 K with uniaxial tension along the y

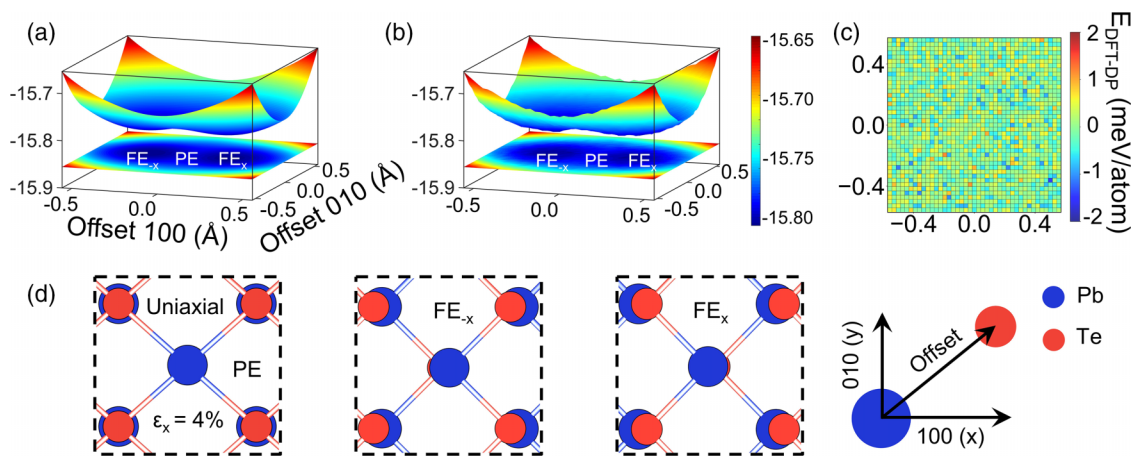


FIG. 4. Energy landscapes of the uniaxially in-plane strained 2D PbTe concerning the offset of the nearest lead and tellurium atoms. Energy landscapes of (a) DFT and (b) the DP model, respectively. (c) Distribution of absolute errors ($E_{\text{DFT-DP}}$) between DFT and the DP model. (d) Structures of the 2D PbTe about the PE (with 4% uniaxial prestrain), the FE with negative polarization, the FE with positive polarization, and the depiction of the offset, respectively.

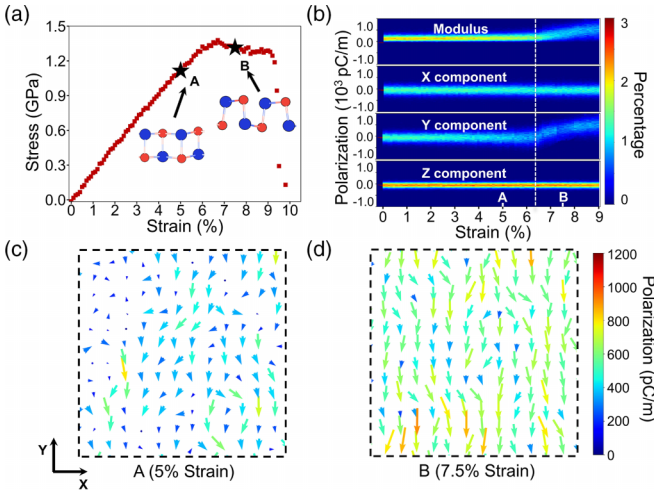


FIG. 5. Uniaxial strain-induced ferroelectric phase transition of 2D PbTe at 300 K. (a) Strain-stress curve during the quasistatic loading process. (b) The modulus and the three components (X , Y , and Z) of it are all provided. The dashed line indicates the position of the phase transition point. (c) Distributions of local polarization with the strain of 5%, corresponding to point A. (d) Distributions of local polarization with the strain of 7.5%, corresponding to point B.

(b) direction using the quasistatic loading procedure described in Sec. II C. Figure 5 presents the strain-stress curve, statistics of local polarization, and snapshots of local polarization. Supplemental Material Fig. S4 [49] also provides the results at 200 K and 100 K. The strain-stress curve [Fig. 5(a)] exhibits a sudden change in slope at a strain of 6.3%, indicating the occurrence of the soft mode instability at the phase transition point of the SIFPT. The modulus of the local polarization [Fig. 5(b)], serving as the order parameter, is zero-centered before the phase transition point and becomes non-zero-centered beyond it, indicating the symmetry breaking of 2D PbTe in the vicinity of this strain at 300 K (from PE to FE transition). It is worth noting that the x and z components of local polarization [Fig. 5(b)] are always zero-centered under strain, suggesting that the change in modulus of local polarization primarily occurs in the y component. Consistent with the statistical analysis, the local polarization is approximately zero in magnitude and randomly orientating in the PE phase [Fig. 5(c)] for point A in Fig. 5(b), but becomes significant and aligned along the y direction in the FE phase [Fig. 5(d)] for point B [Fig. 5(b)]. These findings remain in good agreement with the observations in Fig. 4.

Furthermore, the snapshot [Fig. 5(d)] reveals the existence of long-range FE order beyond the critical strain, indicating that the ferroelectricity of 2D PbTe can withstand the thermal fluctuations at 300 K when subjected to appropriate strain. Fortunately, the critical strain (about 6.3%) of 2D PbTe at 300 K is generally attainable due to the exceptional flexibility of 2D material [22]. Notably, the current MD simulation at 300 K demonstrates the coupling of polarization state and strain conditions, highlighting the potential for FE strain engineering of 2D PbTe at room temperature.

Figure 6 presents the probability distributions of the modulus of local polarization and its components at different

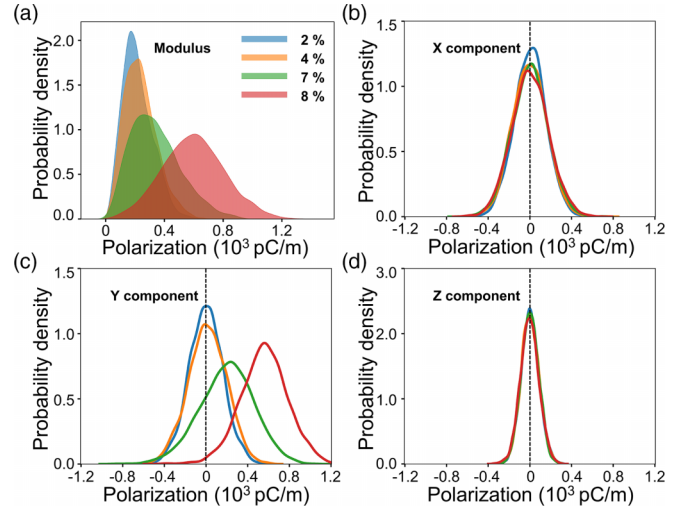


FIG. 6. Probability distributions of local polarization of uniaxially strained 2D PbTe at 300 K with strains of 2%, 4%, 7%, and 8%, respectively. Distributions of polarization in (a) the modulus and the (b) x , (c) y , and (d) z components at corresponding strains, respectively. The dashed lines indicate the positions with zero polarization.

strains at 300 K (refer to the results at 200 K and 100 K in Supplemental Material Fig. S5 [49]). Figure 6(a) shows the probability distribution of the polarization modulus with the uniaxial strains. Before the critical strain, i.e., uniaxial strain smaller than 6%, the probability distribution of the polarization modulus remains unchanged. However, beyond the transition strain (uniaxial strain larger than 6%), the probability distributions of the polarization modulus shift to larger values, suggesting the strain-induced FE phase transition led to significant ferroelectric polarizations. In-depth analysis of the polarization components along x , y , and z directions [as shown in Fig. 6(b), 6(c), and 6(d), respectively] shows only one peak centered in zero polarization at a strain less than the critical value for all three components, revealing the paraelectric phase for 2D PbTe. However, beyond the critical strain, although the x and z components still show the zero-centered characterization of the probability distributions of polarization, the probability distribution profiles of the y component display the non-zero-centered unimodal bell shape. This characteristic shape is typical of a displacive phase transition [56,57], keeping well in agreement with the y component being primarily responsible for the variation in local polarization. It indicates that the symmetry change from the PE to FE phase transition in uniaxially strained 2D PbTe is achieved via the displacement of lead and tellurium atoms along the strain axis.

C. Strain-aided temperature-induced ferroelectric phase transition

It is worth noting that the critical strain for SIFPT in 2D PbTe is approximately 3.75% at 0 K, as determined from our previous DFT calculations. However, in the current MD simulation at 300 K, the critical strain increases to approximately 6.3%. Therefore, it is crucial to establish a strain-temperature phase diagram for 2D PbTe to guide its

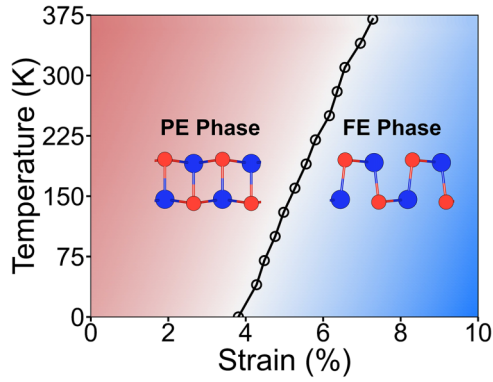


FIG. 7. The strain-temperature ferroelectric phase diagram of 2D PbTe determined by MD simulations with the DP model.

utilization in FE nanodevices. This phase diagram would provide valuable insights into the appropriate strain and temperature ranges for achieving and maintaining the desired ferroelectric properties in practical applications. Figure 7 presents the strain-temperature phase diagram of 2D PbTe constructed by the MD simulations with the DP model. It can be seen that the critical strain of the SIFPT rises with increasing temperature. This result is consistent with the SIFPT of the SrTiO₃ membrane under uniaxial tension [18].

Besides the SIFPT, the TIFPT presents another avenue for the application of ferroelectric materials. By referring to Fig. 7, we can further investigate the temperature effect on the FE transition in 2D PbTe, taking into account the prestrains applied. Here, uniaxial prestrains of 5% and 6.6% were selected along the *y* direction. Subsequently, MD simulations were carried out to simulate the temperature increase procedure from 0 K to 400 K. The evolution of local polarizations

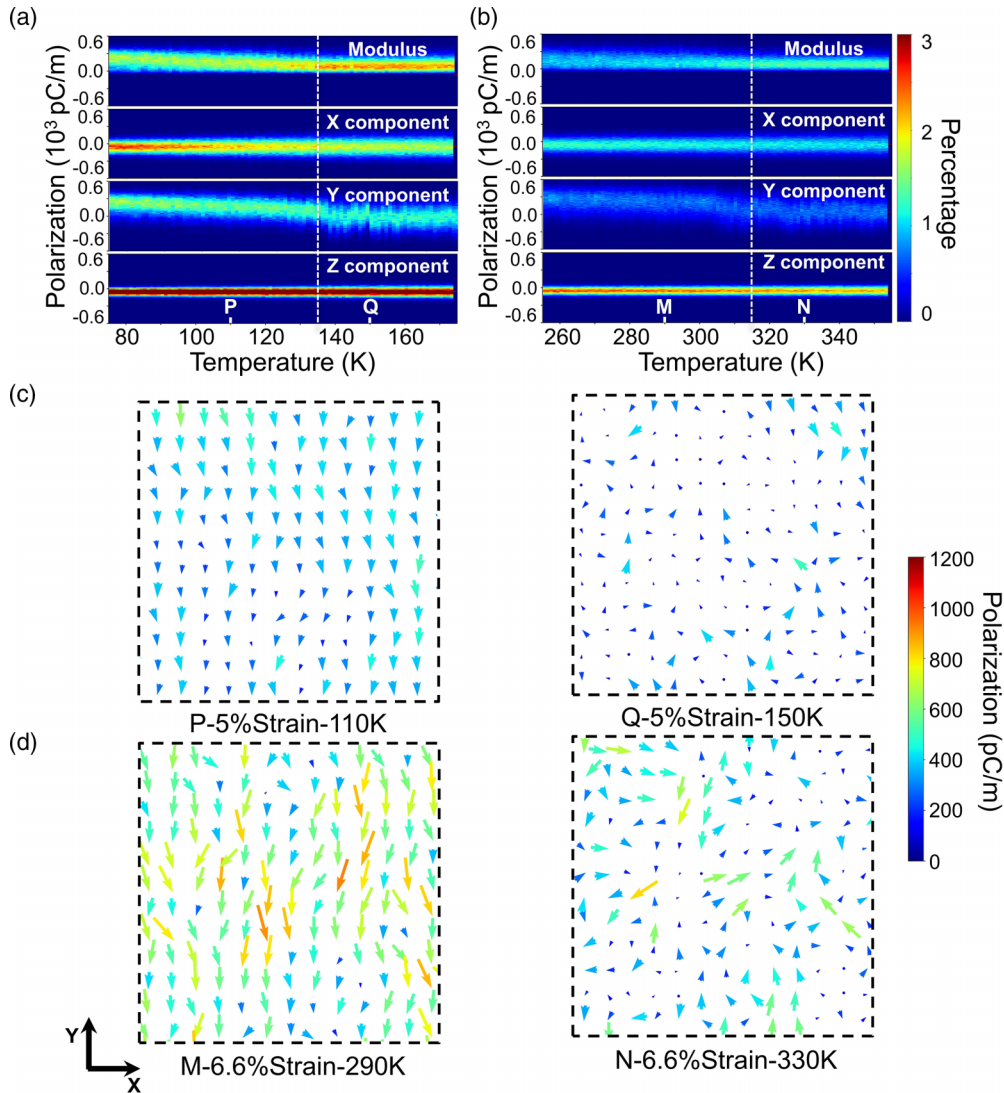


FIG. 8. Temperature-induced ferroelectric phase transition of uniaxially prestrained 2D PbTe. Evolutions of the local polarization with temperature at (a) 5% and (b) 6.6% prestrains. The modulus and the three components (*x*, *y*, and *z*) of it are all provided. The dashed lines indicate the positions of phase transition points. (c) Distributions of local polarization below (110 K, point *P*) and above (150 K, point *Q*) the phase transition temperature of 2D PbTe under 5% prestrains. (d) Distributions of local polarization below (290 K, point *M*) and above (330 K, point *N*) the phase transition temperature of 2D PbTe under 6.6% pre-strains.

and their snapshots during the temperature increase is depicted in Fig. 8.

Figure 8(a) and 8(b) shows the local polarization and its components in the temperature-driven phase transition case, which resembles the behavior of the strain-driven case. The modulus of local polarization approaches zero above the transition temperature and increases continuously below it, indicating symmetry breaking. Owing to the coupling of the prestrain and polarization, the variation of the y component governs the symmetry breaking of this TIFPT in uniaxially prestrained 2D PbTe. The profiles of probability distributions of the y component further confirm the displacive nature of this phase transition (see Supplemental Material Fig. S6 [49]). Meanwhile, the critical temperatures of FE transition in prestrained 2D PbTe can be determined as 135 K and 315 K for strains of 5% and 6.6%, respectively. Figure 8(c) and 8(d) double-confirmed the TIFPT for prestrained 2D PbTe. At the temperature above the transition point [150 K and 330 K for the cases with the prestrains of 5% and 6.6%, as illustrated in Fig. 8(c) and 8(d), right, respectively], the local polarizations exhibit random orientations due to thermal fluctuation and they follow a zero-centered statistical distribution, indicating a PE state. However, at temperatures below the transition point [110 K and 290 K for the cases with the prestrains of 5% and 6.6%, as depicted in Fig. 8(c) and 8(d), left, respectively], the long-range FE ordering emerges from the y -aligned local polarization, showing robust ferroelectricity even at room temperature when appropriate prestrain is applied.

Above TIFPT behavior indicates that the critical temperatures of prestrained 2D PbTe align closely (with errors of about ± 10 K) with the results obtained from the phase diagram, despite being influenced by the applied strains at different temperatures. This demonstrates the convergence and accuracy of our MD calculations. More importantly, we observe a significant elevation in the T_C of strained 2D PbTe, even surpassing room temperature. Moreover, considering the progress in nanotechnology, achieving the necessary prestrain in 2D PbTe is technically feasible [18,58,59]. Therefore, with varying prestrains, the T_C of 2D PbTe can be continuously tuned over a wide temperature range, highlighting its immense potential for applications in miniaturized functional devices such as temperature sensors and motion monitors.

D. Second-order transition characteristics for FE transitions in 2D PbTe

Furthermore, we investigated the cyclic behavior of FE phase transitions in monolayer PbTe, including both strain-induced and temperature-induced transitions. Figure 9 presents the results of a loading/unloading cycle and a heating/cooling cycle for the FE phase transitions. Remarkably, the evolution of polarization during cyclic strain loading, as shown in Fig. 9(a), demonstrates the recoverability of the ferroelectric polarization with the FE transition points coinciding during both the loading and unloading processes at 300 K. Similarly, this behavior is also observed in the case of the temperature-induced ferroelectric phase transition [Fig. 9(b)] during the heating and cooling for the 6.6% prestrained sample. These findings indicate that both the strain-induced and temperature-induced phase transitions in 2D PbTe are

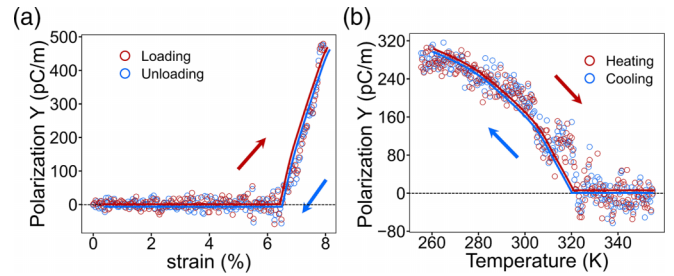


FIG. 9. Evolution of polarization (y direction) during the ferroelectric phase transition cycles of 2D PbTe. (a) A loading/unloading cycle for the ferroelectric phase transition at 300 K. (b) A heating/cooling cycle for the FE phase transitions of PbTe with 6.6% prestrain. The inserted lines are used to guide the eye.

reversible and exhibit no hysteresis. This property is particularly advantageous for devices that require a constant FE transition point under repeated loadings. In addition, the absence of hysteresis in 2D PbTe serves as an observable characteristic, suggesting a feature of the nonfirst-order phase transition [60,61].

Indeed, in the context of FE phase transitions, it is well-known that such transitions typically involve symmetry breaking and result in a structural difference between the PE and FE phases. This structural change could lead to spontaneous strain, which serves as the secondary order parameter [11,62,63]. However, as illustrated in Supplemental Material Fig. S7 [49], both the strain-driven (300 K) and temperature-driven phase transitions (6.6% prestrain) of 2D PbTe exhibit no abrupt change in polarization or lattice constants. The lattice constants (perpendicular to the strain axis) remain consecutive between the PE and FE phases near the transition point. Both the polarization (primary-order parameter) and the strain (secondary-order parameter) exhibit continuity around the transition point without any regions of phase coexistence (as evidenced by the results in Figs. 8 and 5). These findings confirm that both SIFPT and TIFPT in 2D PbTe are not first-order transitions.

To gain further insights, we conducted calculations to determine the change in free energy associated with the strain for SIFPT and the change in enthalpy associated with the temperature for TIFPT, as presented in Fig. 10(a) and 10(b), respectively. The results reveal that the first-order derivatives

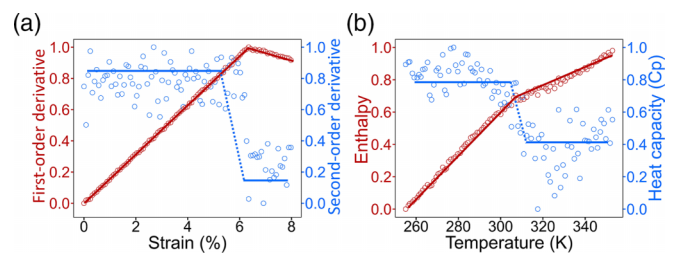


FIG. 10. Evolutions of free energy and enthalpy of phase transition of 2D PbTe over the transition path. (a) Profiles of the derivatives of free energy in SIFPT at 300 K. (b) Profiles of enthalpy and specific heat capacity in TIFPT with a prestrain of 6.6%. The reduced values are applied in all the vertical axes of (a) and (b) for better illustration. The inserted lines are used to guide the eye.

of free energy and the enthalpy remain continuous. In contrast, the second-order derivative of free energy and the specific heat capacity show discontinuities at the transition point. These findings strongly support the second-order nature of both strain-induced and temperature-induced ferroelectric phase transitions in 2D PbTe. This observation is consistent with experimental results obtained from atomic-thin SnTe, which shares a similar structure with 2D PbTe, but exhibits a FE transition at 270 K in the ground state [12].

IV. CONCLUSION

In summary, we developed a deep-learning force field model using the DeePMD-kit package to study the SIFPT and the TIFPT of 2D PbTe at finite temperatures. The accuracy and the generalization performance of our DP model are well testified by predicting the validation configurations, energy landscape concerning the offset of lead and tellurium atoms, and the static properties, demonstrating the ability to predict potential energy reasonably over a wide phase space. With the validated DP model, the existence of the long-range FE order of strained 2D PbTe is observed by our MD simulations at room temperature. Meanwhile, the displacive nature of the

transition via the offset of the nearest lead and tellurium atoms along the strain axis, and the coupling between strain and polarization of 2D PbTe are revealed by the statistics of local polarization. Moreover, the strain-temperature phase diagram of 2D PbTe is determined, and the second-order nature of the FE phase transitions is exposed, inspiring the potential applications of 2D ferroelectric materials for room-temperature nonhysteresis ferroelectricity.

ACKNOWLEDGMENTS

The authors gratefully acknowledge the support of NSFC (Grant No. 11974269), the support of the Key Research and Development Program of Shaanxi (Grant No. 2023-YBGY-480), and the 111 Projects 2.0 (Grant No. BP0618008). J.Z.L. acknowledges the support from ARC discovery projects (Grant No. DP210103888) and HPC from National Computational Infrastructure from Australia. The authors also thank F. Yang and X. D. Zhang at the Network Information Center of Xi'an Jiaotong University for supporting the HPC platform. This work was also supported by the high-performance computing power and technical support provided by Xi'an Future Artificial Intelligence Computing Center.

-
- [1] M. Si, A. K. Saha, S. Gao, G. Qiu, J. Qin, Y. Duan, J. Jian, C. Niu, H. Wang, W. Wu, S. K. Gupta, P. D. Ye, A ferroelectric semiconductor field-effect transistor, *Nat. Electron.* **2**, 580 (2019).
- [2] L. Han *et al.*, High-density switchable skyrmion-like polar nanodomains integrated on silicon, *Nature (London)* **603**, 63 (2022).
- [3] W. Zheng, Y. Xu, L. Zheng, C. Yang, N. Pinna, X. Liu, and J. Zhang, MoS₂ van der Waals $p-n$ junctions enabling highly selective room-temperature NO₂ sensor, *Adv. Funct. Mater.* **30**, 2000435 (2020).
- [4] M. Dai, Z. Wang, F. Wang, Y. Qiu, J. Zhang, C.-Y. Xu, T. Zhai, W. Cao, Y. Fu, D. Jia, Y. Zhou, P.-A. Hu, Two-dimensional van der Waals materials with aligned in-plane polarization and large piezoelectric effect for self-powered piezoelectric sensors, *Nano Lett.* **19**, 5410 (2019).
- [5] C. J. Brennan, R. Ghosh, K. Koul, S. K. Banerjee, N. Lu, and E. T. Yu, Out-of-plane electromechanical response of monolayer molybdenum disulfide measured by piezoresponse force microscopy, *Nano Lett.* **17**, 5464 (2017).
- [6] T. Jin, J. Mao, J. Gao, C. Han, K. P. Loh, A. T. S. Wee, and W. Chen, Ferroelectrics-integrated two-dimensional devices toward next-generation electronics, *ACS Nano* **16**, 13595 (2022).
- [7] S. Yuan, X. Luo, H. L. Chan, C. Xiao, Y. Dai, M. Xie, and J. Hao, Room-temperature ferroelectricity in MoTe₂ down to the atomic monolayer limit, *Nat. Commun.* **10**, 1775 (2019).
- [8] W. Ding, J. Zhu, Z. Wang, Y. Gao, D. Xiao, Y. Gu, Z. Zhang, and W. Zhu, Prediction of intrinsic two-dimensional ferroelectrics in In₂Se₃ and other III₂-VI₃ van der Waals materials, *Nat. Commun.* **8**, 14956 (2017).
- [9] C. Xiao, F. Wang, S. A. Yang, Y. Lu, Y. Feng, and S. Zhang, Elemental ferroelectricity and antiferroelectricity in group-V monolayer, *Adv. Funct. Mater.* **28**, 1707383 (2018).
- [10] J. Gou, H. Bai, X. Zhang, Y. L. Huang, S. Duan, A. Ariando, S. A. Yang, L. Chen, Y. Lu, and A. T. S. Wee, Two-dimensional ferroelectricity in a single-element bismuth monolayer, *Nature (London)* **617**, 67 (2023).
- [11] M. Mehboudi, A. M. Dorio, W. Zhu, A. van der Zande, H. O. H. Churchill, A. A. Pacheco-Sanjuan, E. O. Harriss, P. Kumar, and S. Barraza-Lopez, Two-dimensional disorder in black phosphorus and monochalcogenide monolayers, *Nano Lett.* **16**, 1704 (2016).
- [12] K. Chang, J. Liu, H. Lin, N. Wang, K. Zhao, A. Zhang, F. Jin, Y. Zhong, X. Hu, W. Duan, Q. Zhang, L. Fu, Q.-K. Xue, X. Chen, S.-H. Ji, Discovery of robust in-plane ferroelectricity in atomic-thick SnTe, *Science* **353**, 274 (2016).
- [13] N. Higashitarumizu, H. Kawamoto, C.-J. Lee, B.-H. Lin, F.-H. Chu, I. Yonemori, T. Nishimura, K. Wakabayashi, W.-H. Chang, and K. Nagashio, Purely in-plane ferroelectricity in monolayer SnS at room temperature, *Nat. Commun.* **11**, 2428 (2020).
- [14] H. Wang and X. Qian, Two-dimensional multiferroics in monolayer group IV monochalcogenides, *2D Mater.* **4**, 015042 (2017).
- [15] S. Barraza-Lopez, B. M. Fregoso, J. W. Villanova, S. S. P. Parkin, and K. Chang, Colloquium: Physical properties of group-IV monochalcogenide monolayers, *Rev. Mod. Phys.* **93**, 011001 (2021).
- [16] K. Chang, B. J. Miller, H. Yang, H. Lin, S. S. P. Parkin, S. Barraza-Lopez, Q.-K. Xue, X. Chen, and S.-H. Ji, Standing waves induced by valley-mismatched domains in ferroelectric SnTe monolayers, *Phys. Rev. Lett.* **122**, 206402 (2019).
- [17] D. Pesquera, E. Parsonnet, A. Qualls, R. Xu, A. J. Gubser, J. Kim, Y. Jiang, G. Velarde, Y.-L. Huang, H. Y. Hwang, R. Ramesh, L. W. Martin, Beyond substrates: Strain engineering of ferroelectric membranes, *Adv. Mater.* **32**, 2003780 (2020).

- [18] R. Xu, J. Huang, E. S. Barnard, S. S. Hong, P. Singh, E. K. Wong, T. Jansen, V. Harbola, J. Xiao, B. Y. Wang, S. Crossley, D. Lu, S. Liu, H. Y. Hwang, Strain-induced room-temperature ferroelectricity in SrTiO₃ membranes, *Nat. Commun.* **11**, 3141 (2020).
- [19] S. Barraza-Lopez, T. P. Kaloni, S. P. Poudel, and P. Kumar, Tuning the ferroelectric-to-paraelectric transition temperature and dipole orientation of group-IV monochalcogenide monolayers, *Phys. Rev. B* **97**, 024110 (2018).
- [20] B. Xu, Z. Gong, J. Liu, Y. Hong, Y. Yang, L. Li, Y. Liu, J. Deng, and J. Liu, Tunable ferroelectric topological defects on 2D topological surfaces: Strain engineering skyrmion-like polar structures in 2D materials, [arXiv:2204.05129](https://arxiv.org/abs/2204.05129).
- [21] T. Xu, X. Wang, J. Mai, J. Zhang, J. Wang, and T.-Y. Zhang, Strain engineering for 2D ferroelectricity in lead chalcogenides, *Adv. Electron. Mater.* **6**, 1900932 (2020).
- [22] D. Akinwande, C. J. Brennan, J. S. Bunch, P. Egberts, J. R. Felts, H. Gao, R. Huang, J.-S. Kim, T. Li, Y. Li, K. M. Liechti, N. Lu, H. S. Park, E. J. Reed, P. Wang, B. I. Yakobson, T. Zhang, Y.-W. Zhang, Y. Zhou, Y. Zhu, A review on mechanics and mechanical properties of 2D materials: Graphene and beyond, *Extreme Mech. Lett.* **13**, 42 (2017).
- [23] K. Chang, J. W. D. Villanova, J.-R. Ji, S. Das, F. Küster, S. Barraza-Lopez, P. Sessi, and S. S. P. Parkin, Vortex-oriented ferroelectric domains in SnTe/PbTe monolayer lateral heterostructures, *Adv. Mater.* **33**, 2102267 (2021).
- [24] Y. Yang, H. Zong, J. Sun, and X. Ding, Rippling ferroic phase transition and domain switching in 2D materials, *Adv. Mater.* **33**, 2103469 (2021).
- [25] S. Prosandeev, B. Xu, and L. Bellaiche, Polarization switching in the PbMg_{1/3}Nb_{2/3}O₃ relaxor ferroelectric: An atomistic effective Hamiltonian study, *Phys. Rev. B* **98**, 024105 (2018).
- [26] W. Zhong, D. Vanderbilt, and K. M. Rabe, First-principles theory of ferroelectric phase transitions for perovskites: The case of BaTiO₃, *Phys. Rev. B* **52**, 6301 (1995).
- [27] P. Friederich, F. Häse, J. Proppe, and A. Aspuru-Guzik, Machine-learned potentials for next-generation matter simulations, *Nat. Mater.* **20**, 750 (2021).
- [28] L. Zhang, J. Han, H. Wang, R. Car, and W. E, Deep potential molecular dynamics: A scalable model with the accuracy of quantum mechanics, *Phys. Rev. Lett.* **120**, 143001 (2018).
- [29] A. P. Bartók, M. C. Payne, R. Kondor, and G. Csányi, Gaussian approximation potentials: The accuracy of quantum mechanics, without the electrons, *Phys. Rev. Lett.* **104**, 136403 (2010).
- [30] J. Behler and M. Parrinello, Generalized neural-network representation of high-dimensional potential-energy surfaces, *Phys. Rev. Lett.* **98**, 146401 (2007).
- [31] A. V. Shapeev, Moment tensor potentials: A class of systematically improvable interatomic potentials, *Multiscale Model. Simul.* **14**, 1153 (2016).
- [32] K. T. Schütt, H. E. Sauceda, P.-J. Kindermans, A. Tkatchenko, and K.-R. Müller, SchNet: A deep learning architecture for molecules and materials, *J. Chem. Phys.* **148**, 241722 (2018).
- [33] L. Zhang, J. Han, H. Wang, W. A. Saidi, R. Car, and E. Weinan, End-to-end symmetry preserving inter-atomic potential energy model for finite and extended systems, in *Proceedings of the 32nd International Conference on Neural Information Processing Systems*, NIPS'18 (Curran Associates Inc., Red Hook, NY, 2018), p. 4441–4451.
- [34] P. Xie, Y. Chen, W. Ee, and R. Car, *Ab initio* multi-scale modeling of ferroelectrics: The case of PbTiO₃, [arXiv:2205.11839](https://arxiv.org/abs/2205.11839).
- [35] J. Wu, L. Bai, J. Huang, L. Ma, J. Liu, and S. Liu, Accurate force field of two-dimensional ferroelectrics from deep learning, *Phys. Rev. B* **104**, 174107 (2021).
- [36] R. He, H. Wu, L. Zhang, X. Wang, F. Fu, S. Liu, and Z. Zhong, Structural phase transitions in SrTiO₃ from deep potential molecular dynamics, *Phys. Rev. B* **105**, 064104 (2022).
- [37] S. Plimpton, Fast parallel algorithms for short-range molecular dynamics, *J. Comput. Phys.* **117**, 1 (1995).
- [38] G. Kresse, and J. Furthmüller, Efficiency of ab-initio total energy calculations for metals and semiconductors using a plane-wave basis set, *Comput. Mater. Sci.* **6**, 15 (1996).
- [39] G. Kresse and J. Furthmüller, Efficient iterative schemes for *ab initio* total-energy calculations using a plane-wave basis set, *Phys. Rev. B* **54**, 11169 (1996).
- [40] G. Kresse and D. Joubert, From ultrasoft pseudopotentials to the projector augmented-wave method, *Phys. Rev. B* **59**, 1758 (1999).
- [41] P. E. Blöchl, Projector augmented-wave method, *Phys. Rev. B* **50**, 17953 (1994).
- [42] J. P. Perdew, K. Burke, and M. Ernzerhof, Generalized gradient approximation made simple, *Phys. Rev. Lett.* **77**, 3865 (1996).
- [43] H. Wang, L. Zhang, J. Han, and W. E, DeePMD-kit: A deep learning package for many-body potential energy representation and molecular dynamics, *Comput. Phys. Commun.* **228**, 178 (2018).
- [44] T. Wen, L. Zhang, H. Wang, W. E, and D. J. Srolovitz, Deep potentials for materials science, *Mater. Futures* **1**, 022601 (2022).
- [45] M. Parrinello and A. Rahman, Polymorphic transitions in single crystals: A new molecular dynamics method, *J. Appl. Phys.* **52**, 7182 (1981).
- [46] S. Nosé, A unified formulation of the constant temperature molecular dynamics methods, *J. Chem. Phys.* **81**, 511 (1984).
- [47] A. Barducci, G. Bussi, and M. Parrinello, Well-tempered metadynamics: A smoothly converging and tunable free-energy method, *Phys. Rev. Lett.* **100**, 020603 (2008).
- [48] G. A. Tribello, M. Bonomi, D. Branduardi, C. Camilloni, and G. Bussi, PLUMED 2: New feathers for an old bird, *Comput. Phys. Commun.* **185**, 604 (2014).
- [49] See Supplemental Material at <http://link.aps.org/supplemental/10.1103/PhysRevB.108.134112> for Figs. S1–S7.
- [50] A. Togo and I. Tanaka, First principles phonon calculations in materials science, *Scr. Mater.* **108**, 1 (2015).
- [51] Z. Li, S. Li, J.-P. Castellán, R. Heid, Y. Xiao, L.-D. Zhao, Y. Chen, and F. Weber, Anomalous transverse optical phonons in SnTe and PbTe, *Phys. Rev. B* **105**, 014308 (2022).
- [52] L. Casella and A. Zaccone, Soft mode theory of ferroelectric phase transitions in the low-temperature phase, *J. Phys. Condens. Matter* **33**, 165401 (2021).
- [53] W. Cochran, Crystal stability and the theory of ferroelectricity, *Phys. Rev. Lett.* **3**, 412 (1959).
- [54] R. D. King-Smith and D. Vanderbilt, Theory of polarization of crystalline solids, *Phys. Rev. B* **47**, 1651 (1993).
- [55] K. Chang, F. Küster, B. J. Miller, J.-R. Ji, J.-L. Zhang, P. Sessi, S. Barraza-Lopez, and S. S. P. Parkin, Microscopic manipulation of ferroelectric domains in SnSe monolayers at room temperature, *Nano Lett.* **20**, 6590 (2020).
- [56] B. Zalar, V. V. Laguta, and R. Blinc, NMR evidence for the

- coexistence of order-disorder and displacive components in barium titanate, *Phys. Rev. Lett.* **90**, 037601 (2003).
- [57] Y. Qi, S. Liu, I. Grinberg, and A. M. Rappe, Atomistic description for temperature-driven phase transitions in BaTiO₃, *Phys. Rev. B* **94**, 134308 (2016).
- [58] Z. Dai, L. Liu, and Z. Zhang, Strain engineering of 2D materials: Issues and opportunities at the interface, *Adv. Mater.* **31**, e1805417 (2019).
- [59] Z. Li, Y. Lv, L. Ren, J. Li, L. Kong, Y. Zeng, Q. Tao, R. Wu, H. Ma, B. Zhao, D. Wang, W. Dang, K. Chen, L. Liao, X. Duan, X. Duan, Y. Liu, Efficient strain modulation of 2D materials via polymer encapsulation, *Nat. Commun.* **11**, 1151 (2020).
- [60] H. Kliem, Strain induced change from second order to first order ferroelectric phase transition, *Ferroelectrics* **425**, 54 (2011).
- [61] H.- L. Cai, W. Zhang, J.- Z. Ge, Y. Zhang, K. Awaga, T. Nakamura, and R.- G. Xiong, 4-(Cyanomethyl)anilinium perchlorate: A new displacive-type molecular ferroelectric, *Phys. Rev. Lett.* **107**, 147601 (2011).
- [62] W. Li and J. Li, Ferroelasticity and domain physics in two-dimensional transition metal dichalcogenide monolayers, *Nat. Commun.* **7**, 10843 (2016).
- [63] M. Wu and X. C. Zeng, Intrinsic ferroelasticity and/or multiferroicity in two-dimensional phosphorene and phosphorene analogues, *Nano Lett.* **16**, 3236 (2016).